J. Fluid Mech. (1989), *vol.* 198, *pp.* 345–363
Printed in Great Britain

Three-dimensional knot convection in a layer heated from below

By R. M. CLEVER AND F. H. BUSSE
Institute of Geophysics and Planetary Physics, University of California at Los Angeles, CA 90024, USA
and Institute of Physics, University of Bayreuth, Postfach 10 1251, 8580 Bayreuth, FRG

(Received 30 December 1987)

Steady three-dimensional convection flows induced by the knot instability of two-dimensional convection rolls are studied numerically for various Prandtl numbers. The Galerkin method is used to obtain the three-dimensional solutions of the basic equations in the case of rigid, infinitely conducting boundaries. These solutions exhibit the typical knot-like structure superimposed onto the basic rolls. The Nusselt number and kinetic energy of motion do not differ much for two- and three-dimensional solutions and the toroidal part of the kinetic energy associated with vertical vorticity always remains a small fraction of the total in the case of the knot solution. The analysis of the steady solutions is complemented by a stability analysis with respect to disturbances that fit the same horizontal periodicity interval as the knot solution. All instabilities correspond to Hopf bifurcations. Some example of finite-amplitude oscillatory knot convection are presented.

1. Introduction

In the past few decades the problem of convection in a layer heated from below has played an important role in the progress of our understanding of the evolution of complex flows. Because a number of supercritical bifurcations can be followed experimentally as well as theoretically as the Rayleigh number is increased from its critical value, the successive occupation of new degrees of freedom of motion can be studied in detail. While motions in the form of rolls represent the simplest and most symmetric form of convection, they do not persist as a stable solution of the basic equations for Rayleigh numbers much beyond 2×10^4 in the case of rigid boundaries. An interesting variety of three-dimensional forms of convection replaces the rolls, dependent on the Prandtl number. The predominant examples are bimodal convection at large Prandtl numbers, knot convection at moderate Prandtl numbers and oscillatory convection in low-Prandtl-number fluids. Typical properties of the three-dimensional forms of convection can already be inferred from the stability analysis of rolls as has been discussed, for example, in the reviews by Busse (1978, 1981). Other properties such as the heat transport require the numerical solution of the three-dimensional nonlinear problem. Moreover, the analysis of the stability of the three-dimensional solutions offers the opportunity to identify the third bifurcation of the system if the onset of convection is counted as the first bifurcation.

The nonlinear properties of bimodal and oscillatory convection have been the focus of previous work (Frick, Busse & Clever 1983; Clever & Busse 1987). There has also been considerable interest in the onset of periodic and aperiodic time dependence,

usually confined to the case when the Prandtl number equals unity (Lipps 1976; McLaughlin & Orszag 1982; Grötzbach 1982; Curry *et al.* 1984). But the phenomenon of knot convection has remained unexplored, to our knowledge. Knot convection differs from bimodal convection at high Prandtl numbers in that the momentum advection term plays an important role. Even though the knot instability and the cross-roll instability leading to bimodal cells exhibit the same symmetry, they can be clearly distinguished as two separate maxima of the growth rate as a function of the wavenumber along the roll axis, as is demonstrated in figures 12 and 13 of Bolton, Busse & Clever (1986). For Prandtl numbers between 2 and 10 the knot instability plays a prominent role in limiting the region of stable rolls towards high wavenumbers. The distinct properties of knot convection can be noticed, however, over a much wider range of Prandtl numbers. Knot convection can be regarded as the initial stage of spoke-pattern convection which according to experimental observations is the predominant form of high-Rayleigh-number convection at moderate Prandtl numbers (Busse 1981).

2. Mathematical formulation of the problem

We consider a horizontal fluid layer of thickness d which is heated from below. Using d as lengthscale, d^2/κ as timescale, and $\kappa\nu/\gamma g d^3$ as the scale for the temperature we can cast the basic equations in a dimensionless form. As usual, the symbols ν, κ, γ, and g refer to the kinematic viscosity, the thermal diffusivity, the coefficient of thermal expansion and the acceleration due to gravity, respectively. We shall assume the Boussinesq approximation such that the velocity field can be described by the following general representation for a solenoidal vector field:

$$\boldsymbol{v} = \boldsymbol{\nabla}\times(\boldsymbol{\nabla}\times\boldsymbol{k}\phi)+\boldsymbol{\nabla}\times\boldsymbol{k}\psi \equiv \boldsymbol{\delta}\phi+\boldsymbol{\varepsilon}\psi. \tag{2.1}$$

The unit vector $\boldsymbol{k}$ is directed opposite to gravity and parallel to the z-axis of a Cartesian system of coordinates. The origin is assumed to lie on the midplane of the layer. By taking the z-components of the (curl)^2 and of the curl of the equations of motion we obtain two equations for the scalar functions ϕ and ψ:

$$\nabla^4\Delta_2\phi-\Delta_2\theta = P^{-1}\left\{\boldsymbol{\delta}\cdot[(\boldsymbol{\delta}\phi+\boldsymbol{\varepsilon}\psi)\cdot\boldsymbol{\nabla}(\boldsymbol{\delta}\phi+\boldsymbol{\varepsilon}\psi)]+\frac{\partial}{\partial t}\nabla^2\Delta_2\phi\right\}, \tag{2.2a}$$

$$\nabla^2\Delta_2\psi = P^{-1}\left\{\boldsymbol{\varepsilon}\cdot[(\boldsymbol{\delta}\phi+\boldsymbol{\varepsilon}\psi)\cdot\boldsymbol{\nabla}(\boldsymbol{\delta}\phi+\boldsymbol{\varepsilon}\psi)]+\frac{\partial}{\partial t}\Delta_2\psi\right\}, \tag{2.2b}$$

where Δ_2 denotes the two-dimensional Laplacian, $\Delta_2 \equiv \partial^2/\partial x^2+\partial^2/\partial y^2$. The heat equation for the dimensionless deviation θ of the temperature from the static solution of the problem is given by

$$\nabla^2\theta-R\Delta_2\phi = (\boldsymbol{\delta}\phi+\boldsymbol{\varepsilon}\psi)\cdot\boldsymbol{\nabla}\theta+\frac{\partial}{\partial t}\theta. \tag{2.2c}$$

The Rayleigh number R and the Prandtl number P are defined in the usual way,

$$R = \frac{\gamma g(T_2-T_1)\,d^3}{\nu\kappa}, \quad P = \frac{\nu}{\kappa},$$

where T_1 and T_2 denote the temperatures at the upper and the lower isothermal boundaries. Because of the no-slip conditions at these boundaries, the boundary conditions of the problem are given by

$$\phi = \frac{\partial}{\partial z}\phi = \psi = \theta = 0 \quad \text{at} \quad z = \pm\tfrac{1}{2}. \tag{2.3}$$

Equations (2.2) together with boundary conditions (2.3) can be solved by the Galerkin method. We first consider the problem of three-dimensional steady solutions which are periodic in x and in y. By expanding the dependent variables into complete systems of functions that satisfy the boundary conditions we obtain the following representations:

$$\phi = \sum_{l,m,n} a_{lmn} \cos l\alpha_x x \cos m\alpha_y y g_n(z) \equiv \sum_{l,m,n} a_{lmn} \Phi_{lmn}, \tag{2.4a}$$

$$\psi = \sum_{l,m,n} c_{lmn} \sin l\alpha_x x \sin m\alpha_y y \sin n\pi(z+\tfrac{1}{2}) \equiv \sum_{l,m,n} c_{lmn} \Psi_{lmn}, \tag{2.4b}$$

$$\theta = \sum_{l,m,n} b_{lmn} \cos l\alpha_x x \cos m\alpha_y y \sin n\pi(z+\tfrac{1}{2}) \equiv \sum_{l,m,n} b_{lmn} \Theta_{lmn}, \tag{2.4c}$$

where the summation is extended over the domain $0 \leqslant l, m < \infty, 1 \leqslant n < \infty$. The coefficients $a_{00n}, c_{0mn}, c_{l0n}$ can be set equal to zero without any effect on the velocity field $\boldsymbol{v}$. The functions $g_n(z)$ have been introduced by Chandrasekhar (1961, p. 625). Their definition can also be found in Clever & Busse (1974).

In writing (2.4) we have assumed that ϕ is a symmetric function in x as well as in y. This property is suggested by the symmetry of the knot instability which induces the transition from the basic roll solution to the knot solution. Starting with the x-independent solutions for rolls Busse & Clever (1979) found that the knot instability has the same symmetry properties as a flow in the form of rolls at right angles to the given rolls. In the present analysis the two wavenumbers α_y and α_x will be chosen in accordance with the region of predominant knot instability in the (R, P, α_y)-space as shown in the paper by Bolton *et al.* (1986). The equations (2.2) require, of course, that ϕ and θ have the same symmetry with respect to x and y, while ψ has the opposite symmetry. There is yet another symmetry that is useful in reducing the computational effort. Since the basic roll solutions exhibit non-vanishing coefficients a_{0mn} only for even $m+n$, the knot instability induces non-vanishing coefficients a_{lmn} for odd m and n. Thus the knot solution is characterized by the property that the coefficients a_{lmn} and b_{lmn} vanish unless $l+m+n$ is an even integer. The corresponding non-vanishing coefficients c_{lmn} are characterized by an odd sum $l+m+n$.

After inserting (2.4) into the basic equations (2.2) we obtain algebraic equations for the coefficients a_{ijk}, b_{ijk}, and c_{ijk} by multiplying (2.2*a*, *b*, *c*) with the functions Φ_{ijk}, Ψ_{ijk}, and Θ_{ijk}, respectively, and averaging the result over the fluid layer. There is no need to write down the algebraic equations explicitly. They are of the same form as equations (2.12) of Busse & Frick (1985). In order to obtain an approximate numerical solution of the infinite system of algebraic equations, it has to be truncated. Following the procedure used in the recent study of oscillatory convection by Clever & Busse (1987) we neglect all coefficients and corresponding equations with indices satisfying the condition

$$i+j+k > N_{\mathrm{T}}. \tag{2.5}$$

Typically an even integer N_T will be selected although this choice discriminates against the representation for ψ. But since the coefficients c_{ijk} are generally smaller than corresponding coefficients a_{ijk} the choice of an even truncation parameter seems to be justified. For prescribed values of the parameters R, P, α_x and α_y the truncated system of algebraic equations is solved by the Newton–Raphson iteration method. A good initial guess for the coefficients is usually required in order to achieve convergence to the desired three-dimensional solution. Usually the initial guess is given by a neighbouring solution and the parameters R, P, α_x, and α_y can thus be varied only in sufficiently small steps. The first solution has been obtained by starting with the two-dimensional solution in the form of rolls with the eigenvector of the knot instability superimposed onto it. Since the amplitude of the eigenvector is not determined by the stability analysis, a suitable trial value must be chosen. The general experience has been that much closer initial guesses are required for three-dimensional solutions than for two-dimensional solutions with the same value of N_T. Once converged solutions have been obtained, it is usually not difficult to increase N_T until properties of the solutions that are sensitive to N_T, such as the Nusselt number, no longer change by more than 1%. Computer expenses, of course, put a limit on the maximal value of N_T that can be used. Since the number of equations increases roughly with N_T^3, computations become uneconomical beyond $N_T = 14$, in which case a total of 770 equations have to be solved simultaneously. Only at the highest values of the Rayleigh numbers used did the difference of Nusselt number for $N_T = 12$ and $N_T = 14$ exceed 1%. Other global quantities such as the average kinetic energy of motions show much less variation with N_T than the Nusselt number. The same is true for the coefficients in (2.4), at least for relatively low values of l, m and n.

Although the Galerkin method employed in the present numerical analysis becomes less economical than other methods for $N_T \gtrsim 12$, it offers the advantage that the numerous symmetry properties of the steady solution can be easily incorporated in the analysis. In addition the stability of the steady solution can be investigated readily. Such an analysis requires a considerable computational expense when other numerical methods are used and thus is usually omitted. To study the stability of the steady solutions of the form (2.4) we superimpose infinitesimal three-dimensional disturbances $\tilde{\phi}, \tilde{\psi}, \tilde{\theta}$ onto the steady solution. A general representation of these disturbances is given by

$$\tilde{\phi} = \sum_{lmn} \tilde{a}_{lmn} \exp\{\mathrm{i}(l\alpha_x + d)\, x + \mathrm{i}(m\alpha_y + b)\, y + \sigma t\}\, g_n(z), \tag{2.6a}$$

$$\tilde{\psi} = \sum_{lmn} \tilde{c}_{lmn} \exp\{\mathrm{i}(l\alpha_x + d)\, x + \mathrm{i}(m\alpha_y + b)\, y + \sigma t\} \sin n\pi(z + \tfrac{1}{2}), \tag{2.6b}$$

$$\tilde{\theta} = \sum_{lmn} \tilde{b}_{lmn} \exp\{\mathrm{i}(l\alpha_x + d)\, x + \mathrm{i}(m\alpha_y + b)\, y + \sigma t\} \sin n\pi(z + \tfrac{1}{2}), \tag{2.6c}$$

where the coefficients $\tilde{a}_{lmn}, \tilde{c}_{lmn}, \tilde{b}_{lmn}$ are complex numbers and the summation indices l, m run through all integers. Since the experimental evidence suggests that the horizontal periodicity interval of the knot solution is not changed by the instabilities in general, we shall restrict our attention to the case when the Floquet wavenumbers d and b vanish. This restriction offers the advantage that the disturbances separate into several subclasses because of the symmetry of the steady solution. In fact, without this separation into subclasses the stability matrices become so huge, based on the truncation condition

$$|l| + |m| + n > N_T \tag{2.7}$$

in analogy to the corresponding condition (2.5) for the steady solution, that a numerical computation of the eigenvalue σ is not feasible for $N_T \geqslant 12$.

There are three different symmetry properties according to which the general manifold (2.6) of disturbances can be separated into eight subclasses in the special case $b = d = 0$. The first symmetry property actually applies in the general case. Because the steady solution exhibits non-vanishing coefficients a_{lmn} only for even $l+m+n$, the disturbances (2.6) separate into a class with even $l+m+n$ and into a class with odd $l+m+n$. These two classes will be distinguished by the letters E and O. The two other symmetry classifications follow from the symmetry of the function ϕ in x and y. Thus the class of disturbances that is symmetric in x can be separated from the class that is antisymmetric in x provided the Floquet wavenumber d vanishes. The same property holds with respect to the y-dependence. In order to benefit from this property the general representation (2.6) has been replaced by one in which trigonometric functions are used. The eight classes of disturbances are denoted by

$$\text{ECC, ECS, ESC, ESS, OCC, OCS, OSC, OSS} \tag{2.8}$$

where the second letter indicates that the x-dependence of $\tilde{\phi}$ is described by $\cos l\alpha_x x$ (C) or by $\sin l\alpha_x x$ (S) and the third letter indicates the corresponding property for the y-dependence. As in the case of the steady solution, $\tilde{\theta}$ has the same symmetries as $\tilde{\phi}$, while $\tilde{\psi}$ always has the opposite symmetries.

With the separation (2.8) into eight subclasses the stability matrices from which the eigenvalues σ must be derived attain a rank that is comparable with the number of non-vanishing coefficients a_{lmn}, etc. of the steady solution. Among the eigenvalues σ only the one with the largest real part is of interest. At the point where σ_r becomes positive as a function of R (or as a function of α_x, α_y) the steady solution becomes unstable. As long as all eigenvalues σ have negative or vanishing real parts the steady solution is considered to be stable.

3. Steady knot convection

As the Rayleigh number increases beyond the stability boundary for the onset of the knot instability, the two-dimensional rolls are modified only slightly at first by the growing knot disturbance, as is evident from the left side of figure 1. Because the maxima in the y-direction of the vertical velocity are not shifted, the boundaries of the rolls remain unchanged. At higher Rayleigh numbers, however, the sinusoidal distortion of the isotherms has given way to the formation of highly concentrated rising and falling plumes as shown by figure 1 (*b*) (ii). This concentration is less visible in the picture of the vertically averaged temperature which includes the contributions from the boundary layers at both ends of the plumes. The star-like spread of the hot isotherms near the bottom boundary indicates that the rising plume is formed in part through the advection of 'thermal ridges' in the bottom boundary layer. This phenomenon will become even more evident in the discussion below of the velocity field.

In order to present the characteristic features of knot convection we have chosen relatively high Rayleigh numbers at which the steady solution is usually unstable, as will be discussed in the following section. While the instabilities introduce a time dependence, the time average of the solutions remains quite close to the steady solutions. The latter are thus still of physical interest in the regime where they are unstable. The form of the knot solutions depends much more on the Rayleigh

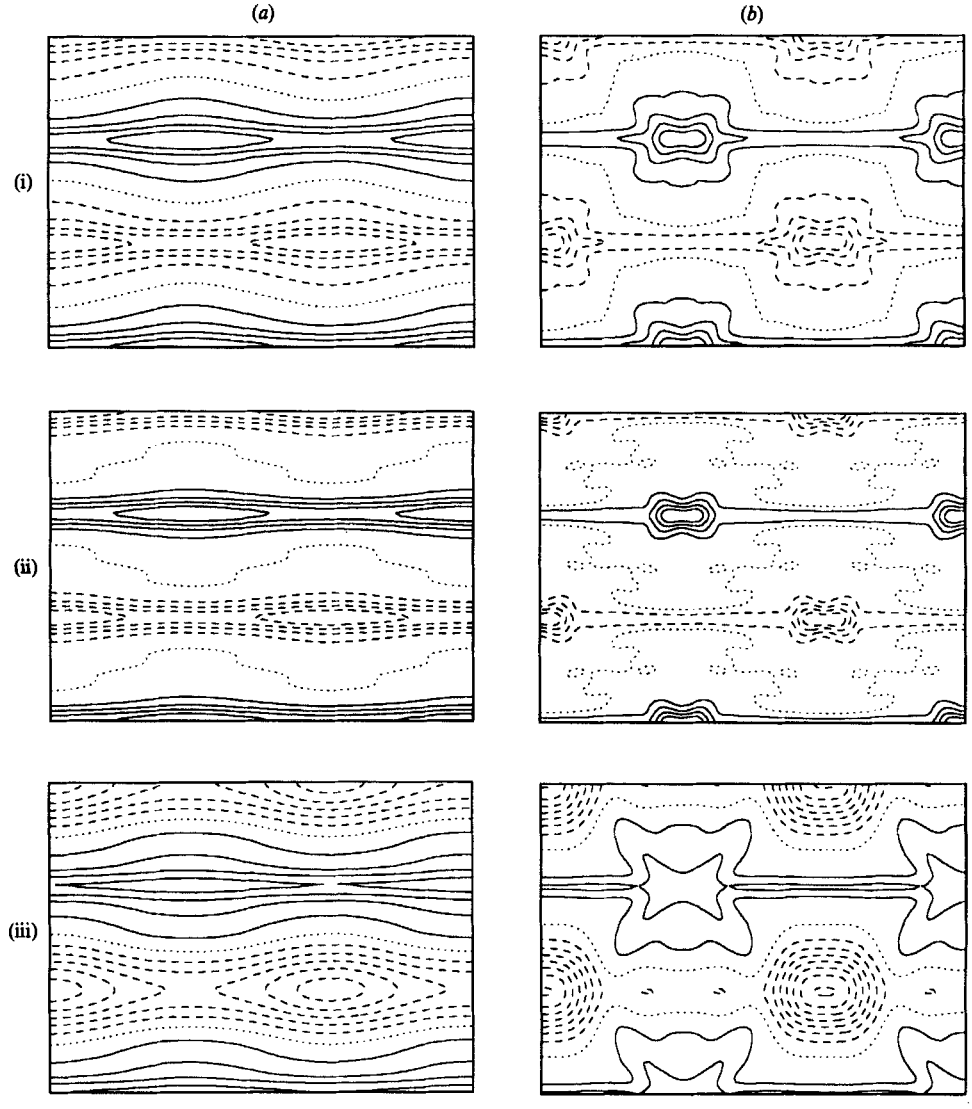

FIGURE 1. Isotherms of steady knot convection at Rayleigh numbers (*a*) $R = 2.5 \times 10^4$ and (*b*) $R = 8 \times 10^4$ for $P = 7$. Rows (i), (ii) and (iii) describe the isotherms of the temperature averaged over the height of the layer $\int \theta \, dz$, the temperature on the median plane $\theta(x, y, 0)$, and the z-derivative $\partial_z \theta$ at the lower boundary, respectively. Only the deviation from the horizontal mean is shown; $\alpha_x = 1.8, \alpha_y = 2.5$ are the wavenumbers. Solid (dashed) lines describe positive (negative) values at $n/5$ of the extremal values, $n = 1, 2, 3, 4$, while the dotted line indicates the zero-isotherm. The same notation is used in the following figures.

number than on the Prandtl number. Since the knot instability sets in at lower Rayleigh numbers for lower Prandtl numbers, the evolution of its finite-amplitude properties also occurs faster with increasing Rayleigh number when P is lower. The asymmetry between rising plumes and the thin rising sheets of hot fluid between them is evident from figure 2; the small wiggles on the isotherms in the high-Rayleigh-number case indicate a local limitation of the numerical approximation.

The difference between rolls and knot solutions in the advection of the temperature field is also expressed by the profiles of the horizontally averaged temperature as

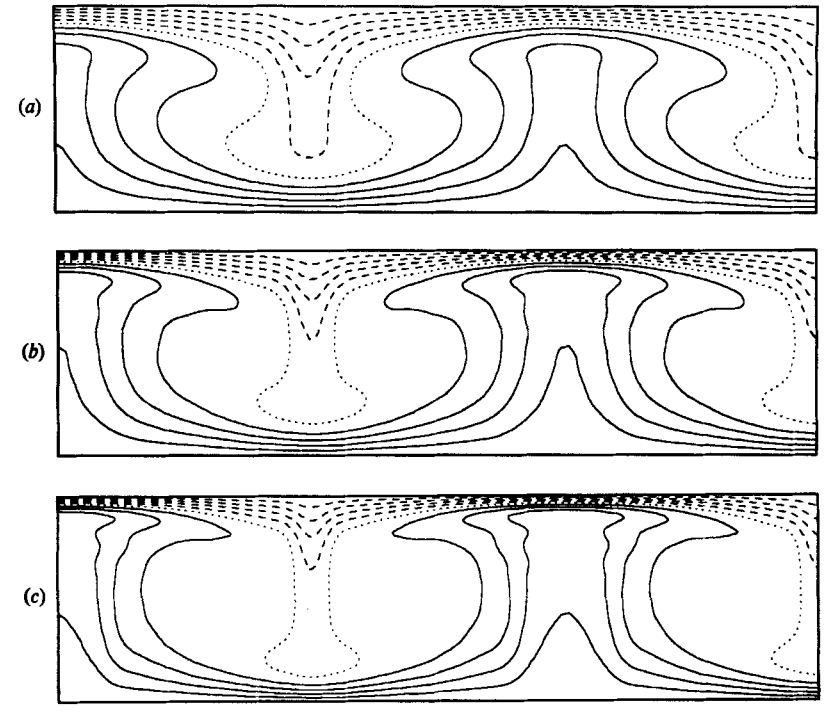

FIGURE 2. The isotherms in a vertical cross-section $y = 0$, for $P = 2.5$ at the Rayleigh numbers (*a*) $R = 1.5 \times 10^4$, (*b*) $R = 4 \times 10^4$, (*c*) $R = 10^5$. The wavenumbers are $\alpha_x = 1.8, \alpha_y = 2.5$.

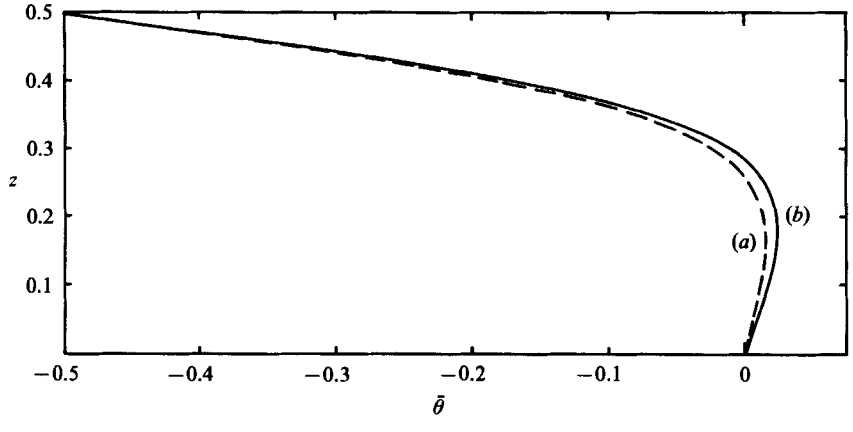

FIGURE 3. The profiles of the horizontally averaged temperature for the knot solution (*a*) and the roll solution (*b*) in the case $R = 4 \times 10^4, P = 4$. Since the profiles are antisymmetric in z, only the upper half is shown.

shown in figure 3 for $P = 4.0$. The typical reversal of the mean temperature gradient in the interior is reduced to about $\frac{3}{5}$ of its value in the case of rolls. The concentrated rising plumes of the knot solution spread over a smaller area than the rising sheets of roll convection as they reach the upper boundary. Ultimately the intricate structure of the knot solution permits a higher heat transport than in the case of the two-dimensional rolls, as we shall discuss below.

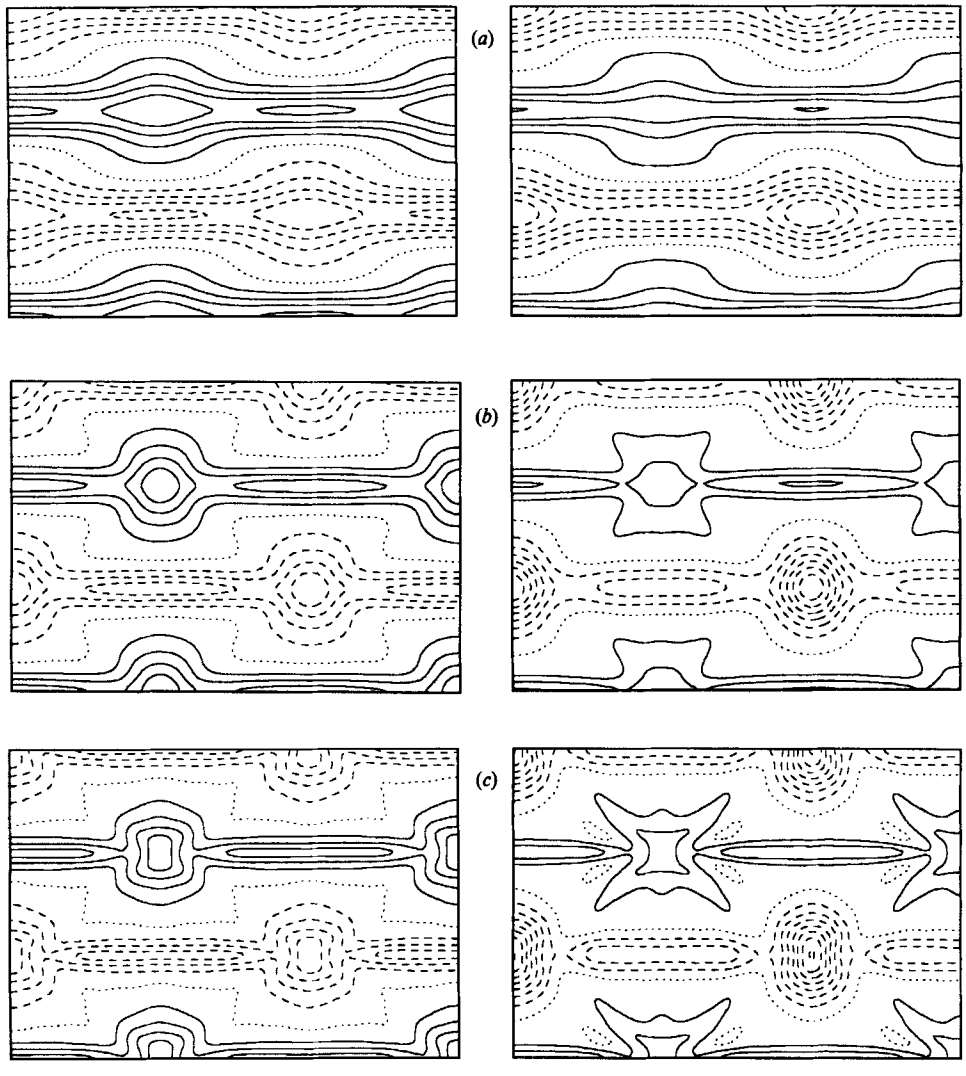

FIGURE 4. The lines of constant vertical velocity in the planes $z = 0$ (left) and $z = -0.3$ (right) for the same three cases as in figure 2.

The evolution of the velocity field as function of the Rayleigh number is shown in figure 4. While the concentration of the vertical velocity in the narrow rising and falling plumes is not as pronounced as in the case of the temperature field, the rising ridges near the lower boundary become well established with increasing Rayleigh number. The pictures discussed so far indicate the characteristic eruptions from the thermal boundary layers and the collection of these ridges into the narrow plumes. Figure 5 shows the velocity field for the two cases for which the temperature field was described in figure 1. Because of the higher Rayleigh and Prandtl numbers the narrowness of plumes and sheets appears to be accentuated in comparison to the curves of figure 3. But in all qualitative respects the velocity fields appear to be very similar. In figure 5 the streamlines of the toroidal component of the velocity field have also been displayed. The toroidal component vanishes in the case of two-dimensional rolls and is generated through the three-dimensional momentum

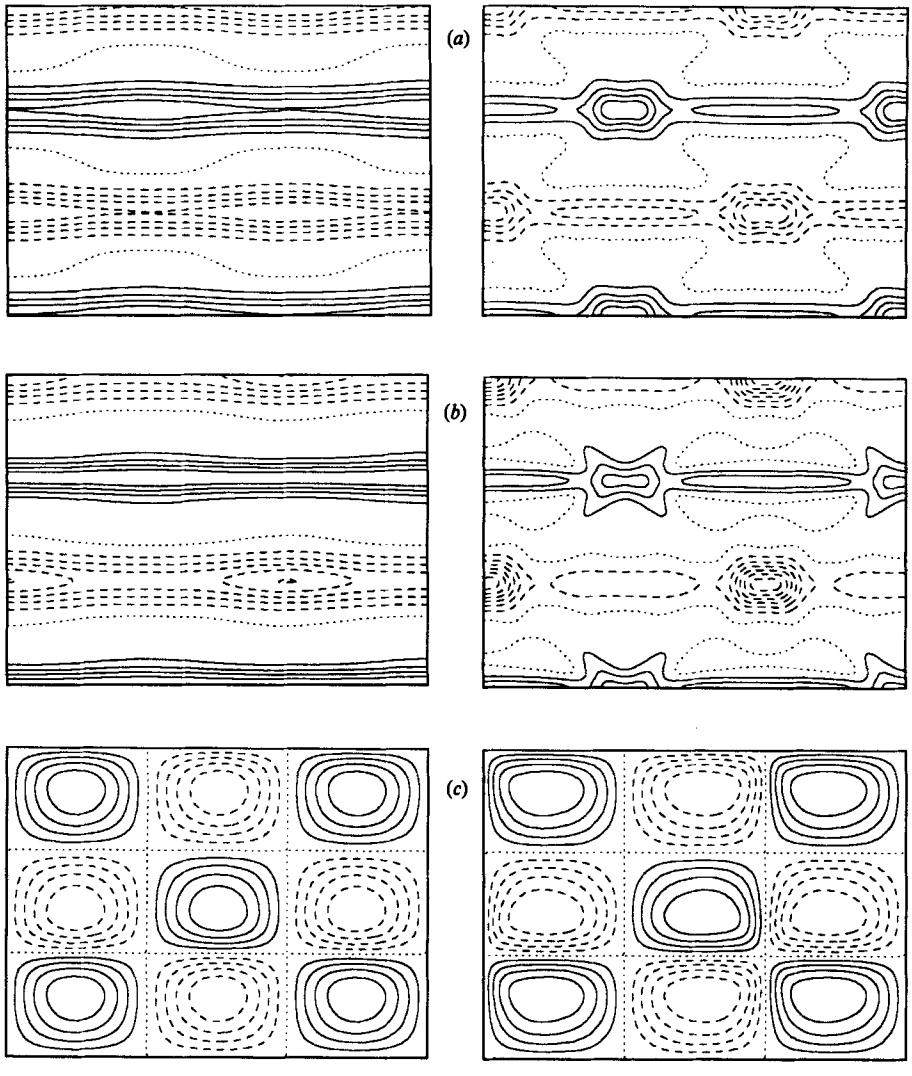

FIGURE 5. The lines of constant vertical velocity in the planes (*a*) $z = 0$ and (*b*) $z = -0.3$ and (*c*) the lines of constant ψ in the plane $z = -0.3$ for $R = 2.5 \times 10^4$ (left) and $R = 8 \times 10^4$ (right) with $\alpha_x = 1.8, \alpha_y = 2.5, P = 7$.

advection by the poloidal component. Because the amplitude of ψ is very small, the toroidal velocity field has a more subtle effect on the dynamics of knot convection.

Figures 6, 7, and 8 show the heat transport by steady knot convection in comparison with that of rolls. Also shown is the kinetic energy of the poloidal component of motion,

$$E_{\text{pol}} \equiv \tfrac{1}{2}\langle|\nabla \times (\nabla \times \boldsymbol{k}\phi)|^2\rangle. \tag{3.1}$$

The Nusselt numbers for the knot solution and the corresponding two-dimensional solution are actually rather close and a fine scale has to be used to distinguish the curves in the plots. As can be seen from the cases of different wavenumbers α_y, the heat transport differs more for different wavelengths than between three- and two-dimensional solutions at a given wavelength $2\pi/\alpha_y$. While the Nusselt number of the

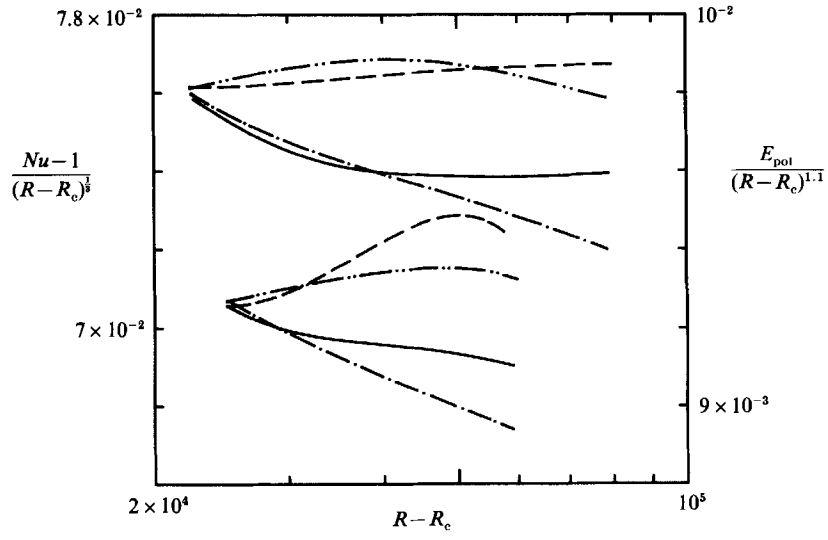

FIGURE 6. Nusselt number for rolls (–·–) and for knots (——), and kinetic energy E_{pol} for rolls (–· ·–) and for knots (– – –) as functions of the Rayleigh number in the case $P = 7.0$. The upper set of curves correspond to $\alpha_x = 1.8, \alpha_y = 2.5$, the lower set to $\alpha_x = 1.6, \alpha_y = 2.0$.

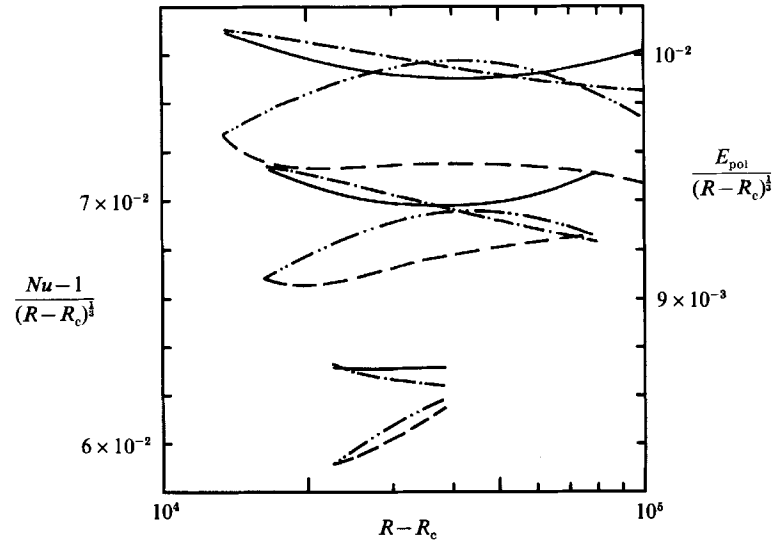

FIGURE 7. Same as figure 6 but for $P = 4.0$. The uppermost set of four curves corresponds to $\alpha_x = 1.7, \alpha_y = 2.5$, the intermediate set to $\alpha_x = 1.5, \alpha_y = 2.0$, and the set at the bottom to $\alpha_x = 1.2$, $\alpha_y = 1.5$.

knot solution drops slightly below that of the roll solution after the bifurcation, this relationship becomes reversed as the Rayleigh number increases. At the higher Prandtl numbers it is not even clear whether the Nusselt number for knots is always lower than that of rolls at the point of bifurcation, because the two values do not match exactly at the point of bifurcation for numerical reasons. The two-dimensional solution is usually computed at a higher level of truncation than the three-dimensional one.

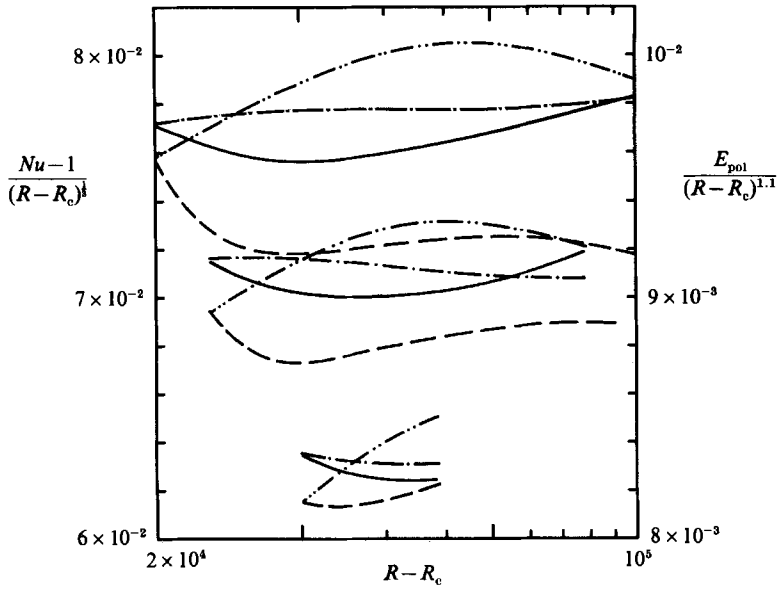

FIGURE 8. Same as figure but for $P = 2.5$. The uppermost set of four curves corresponds to $\alpha_x = 1.7, \alpha_y = 2.5$, the intermediate set to $\alpha_x = 1.4, \alpha_y = 2.0$, and the set at the bottom to $\alpha_x = 1.1$, $\alpha_y = 1.5$.

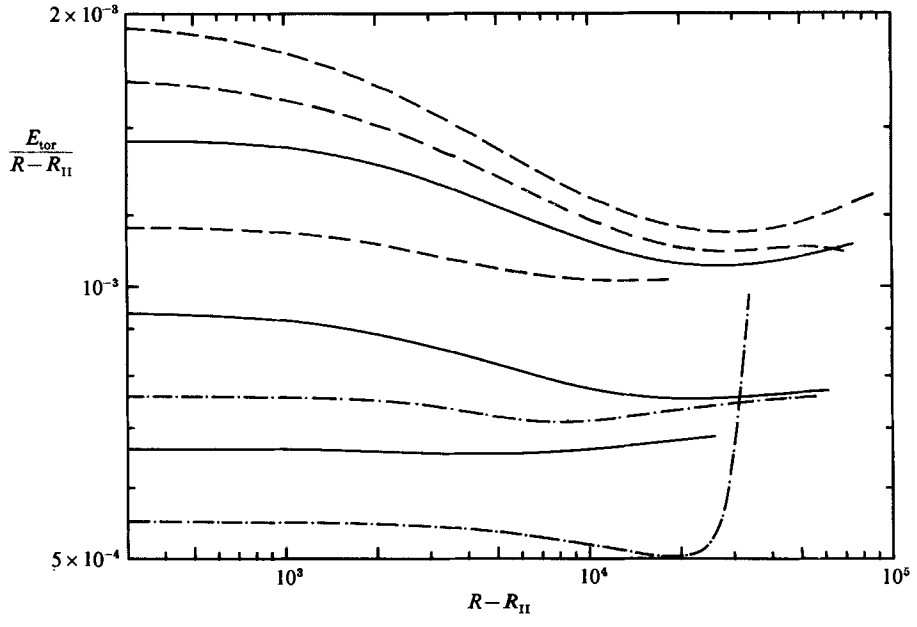

FIGURE 9. The kinetic energy of the toroidal component of knot convection as a function of the Rayleigh number for the Prandtl numbers $P = 2.5$ (– – –), $P = 4.0$ (——), and $P = 7.0$ (– · –). The curves for a given Prandtl number correspond to different wavenumber combinations and their sequence from top to bottom on the left-hand side is the same as in figures 6, 7 and 8, respectively.

The change in the kinetic energy is much more pronounced than the change in the Nusselt number, and the kinetic energy also recovers much more slowly than the heat transport with increasing Rayleigh number. The kinetic energy of knot convection is still smaller than the kinetic energy of rolls if the kinetic energy of the toroidal component,

$$E_{\text{tor}} \equiv \langle |\nabla \times \boldsymbol{k}\psi|^2 \rangle, \tag{3.2}$$

is included except in the case of $P = 7$. Only as the Rayleigh number is increased far beyond the critical value R_{II} does the total kinetic energy of knot convection exceed that of rolls.

The toroidal kinetic energy (3.2) is shown in figure 9 as a function of the Rayleigh number for different Prandtl numbers and wavenumbers. It increases nearly linearly beyond the point of bifurcation, $R = R_{\text{II}}$, but remains small in comparison with the poloidal kinetic energy. The meaning of the sudden upturn of the curve for $\alpha_y = 2.0$, $P = 7$ at the high-Rayleigh-number end has not found an explanation yet. But it does not seem to be caused by the numerical truncation.

Through the development of small scales in the form of eruptions from the thermal boundary layers and in the form of narrow plumes the knot-convection flow ultimately achieves a higher heat transport than can be carried by convection in the form of rolls. But in contrast to the onset of bimodal convection in a high-Prandtl-number fluid, which can be interpreted in terms of the instability of the thermal boundary layers (Busse 1967), the onset of knot convection is a much more complex problem which cannot be explained in simple terms. While the potential energy residing in the thermal boundary layers certainly contributes to the development of small-scale structures near the boundaries, a major influence is the strong momentum advection into the narrow plumes. This advection gives rise to an efficient heat transfer at the opposite boundary as is indicated by the small area of negative $\partial(\theta - \bar{\theta})/\partial z$ in figure 1 (*b*)(iii). A correspondingly larger area is thus available for the formation of the hot plume.

4. Instabilities of steady knot convection

As has already been mentioned in §2, the stability analysis is carried out with respect to periodicity-preserving disturbances with vanishing b, d. From the experimental evidence (Busse & Clever 1979) it appears that wavelength-changing instabilities are not important. This observation is not surprising since the horizontal periodicity interval of knot convection is relatively large. As will be seen below, typical instabilities introduce small-scale structures arising from the thermal boundary layers.

Although the manifold of possible disturbances is significantly reduced by the assumption of vanishing Floquet parameters, there is still a bewildering variety of instabilities. In table 1 a number of instabilities are listed for the steady solutions studied in the preceding section. In addition to the instabilities occurring at the lowest Rayleigh number R_{III} we have listed other instabilities which occur close to this value. The cases with the lowest values of the wavenumbers α_x, α_y have not been included in table 1 because the steady solution is always unstable. In fact the oscillatory instabilities precede the transition to the steady knot solution in those cases, as can be seen from figures 5 and 12 of Bolton *et al.* (1986). Once a steady knot solution becomes established with a finite amplitude, the growth rates of competing instabilities increase much more slowly with increasing Rayleigh number and the

P	α_x	α_y	R_{II}	R_{III}	σ_{i}	Mean flow	Symm.
2.5	1.7	2.5	11589	31987	63.4	N	OSS
				36975	88.9	R	ECS
				37422	89.6	U	ECS
2.5	1.4	2.0	14541	29649	52.1	U	OSC
				29896	70.2	R	ECS
				30022	70.5	U	ECS
4.0	1.7	2.5	14911	38814	192.6	R	ESC
				38802	192.5	U	ESC
4.0	1.5	2.0	17761	29890	147.2	U	ESC
				29921	147.4	R	ESC
				35161	180.2	N	OCC
				35243	227.9	U	OSC
				36065	231.6	N	ECC
7.0	1.8	2.5	23641	33791	224.1	N	OCC
				34341	212.3	U	ESC
				34365	212.4	R	ESC
				39454	240.0	N	ECC

TABLE 1. Instabilities of stationary knot solutions with given wavenumbers α_x, α_y. R_{III} is the critical Rayleigh number for the onset of the instability and σ_{i} is its frequency. The symmetry is defined according to classification (2.9); N, R, U indicate no, restricted, unrestricted mean flow.

onset of oscillatory instabilities occurs at relatively high values for R_{III} as can be seen from the table.

Before we continue to discuss the properties of the instabilities, we must deal with a property of the disturbances (2.6) in the limit $d = b = 0$. In the case $b = d = 0$ the coefficients $\tilde{a}_{00n}$ and $\tilde{c}_{00n}$ do not contribute to the disturbance velocity field and the stability equations are satisfied independently of the values of $\tilde{a}_{00n}$ and $\tilde{c}_{00n}$ which therefore can be set equal to zero. The velocity field described by the coefficients $\tilde{a}_{00n}$ and $\tilde{c}_{00n}$ in the limit of vanishing b and d becomes a mean flow which is not described by the representation (2.6) in the case $b = d = 0$. For this reason we shall exclude the case $l = m = 0$ in the summations (2.6*a*, *b*) and instead add mean flow components to the representation (2.6),

$$U_{x,y} = \sum_n U_n^{(x,y)} \sin n\pi(z+\tfrac{1}{2}) \exp\{\sigma t\}, \tag{4.1a}$$

where the coefficients $U_n^{(x)}, U_n^{(y)}$ are given by

$$U_n^{(x)} = -(n\pi P)^{-1} \mathrm{e}^{-\sigma t} \int_{-\frac{1}{2}}^{\frac{1}{2}} 2 \cos n\pi(z+\tfrac{1}{2}) [\overline{\Delta_2 \phi(\partial_{xz}\tilde{\phi} + \partial_y \tilde{\psi})} + \overline{\Delta_2 \tilde{\phi}(\partial_{xz}\phi + \partial_y \psi)}] \mathrm{d}z$$
$$+ \eta^{(x)}(1-(-1)^n) 2/(n\pi)^3, \tag{4.1b}$$

$$U_n^{(y)} = -(n\pi P)^{-1} \mathrm{e}^{-\sigma t} \int_{-\frac{1}{2}}^{\frac{1}{2}} 2 \cos n\pi(z+\tfrac{1}{2}) [\overline{\Delta_2 \phi(\partial_{yz}\tilde{\phi} - \partial_x \tilde{\psi})} + \overline{\Delta_2 \tilde{\phi}(\partial_{yz}\phi - \partial_x \psi)}] \mathrm{d}z$$
$$+ \eta^{(y)}(1-(-1)^n) 2/(n\pi)^3. \tag{4.1c}$$

The bar indicates the horizontal average and the constant η represents a constant pressure gradient which we have introduced to take into account the possible effect of distant sidewalls on the mean flow. Unlike the fluctuating component of the

velocity field, which may be affected over the distance of one wavelength by the presence of a sidewall, the mean flow will be influenced over much larger distances. Assuming two extreme cases we require that $\eta^{(x,y)}$ either vanishes or is determined by the condition that the vertically averaged mean flow vanishes,

unrestricted mean flow: $\eta^{(x,y)} = 0,$ (4.2*a*)

restricted mean flow: $\eta^{(x,y)}$ is determined by the condition

$$\sum_n U_n^{(x,y)}(1-(-1)^n)/n\pi = 0. \quad (4.2b)$$

The symmetry of the disturbances (2.7) requires that non-vanishing mean-flow coefficients $U_n^{(x)}, U_n^{(y)}$ can be expected only when $\tilde{\phi}, \tilde{\theta}$ are described by sin-functions in the x- or y-directions, respectively. Only disturbances with SC or CS in list (2.8) are thus associated with a mean-flow component. The mean-flow profile $U_{x,y}$ is antisymmetric in z for even disturbances like ESC or ECS, while it is symmetric in z for OSC, OCS. Only in the latter case can a mean pressure gradient be generated.

In considering the instabilities listed in table 1 we can distinguish two classes: the blob instabilities which exhibit the same symmetry in the y-direction as the basic roll solution; and the shift instabilities which have the opposite symmetry in the y-direction and tend to shift the basic roll in the transverse direction. As is evident from the table, the blob instabilities predominate at $P = 4$ and $P = 7$, while the shift instabilities occur only in the low-Prandtl-number cases. The blob instabilities are essentially equivalent to the BO2-instability of rolls (Bolton *et al.* 1986), which is also indicated by the relatively high values of the frequency σ_i. In the cases of OCC and OSC the dominant terms are $\cos 2\alpha_x x$ and $\sin 2\alpha_x x$, respectively. In this way the symmetry corresponds to the symmetry of the BO2-instability. Because rolls are x-independent, the BO2-instability can be described by either $\sin \alpha_x x$ or $\cos \alpha_x x$. In the case of the knot solution the translational invariance in the x-direction no longer exist, but $\sin \alpha_x x$- and $\cos \alpha_x x$-type disturbances still have similar growth rates as is evident from the table.

It is worth noting that the mean flow has very little influence on the growth of instabilities. The Rayleigh numbers R_{III} and the frequencies σ_i for restricted and unrestricted cases are very close and, as we have just mentioned, the replacement of $\sin \alpha_x x$-terms by $\cos \alpha_x x$-terms also has little influence even though there is a mean flow associated with the instability in one case, but not in the other.

5. Oscillatory knot convection

Since all instabilities of the steady knot solution occur in the form of Hopf bifurcations, a new numerical method must be employed in order to follow in time the evolving solutions. By replacing the representation (2.4*a*) by either

$$\phi^{ECC} = \sum_{l,m,n} a_{lmn}(t) \cos l\alpha_x x \cos m\alpha_y y g_n(z), \quad (5.1a)$$

or

$$\phi^{ESC} = \sum_{l,m,n} [a_{lmn}(t) \cos l\alpha_x x + \tilde{a}_{lmn}(t) \sin l\alpha_x x] \cos m\alpha_y y g_n(z), \quad (5.1b)$$

or

$$\phi^{ECS} = \sum_{l,m,n} \cos l\alpha_x x [a_{lmn}(t) \cos m\alpha_y y + \tilde{a}_{lmn}(t) \sin m\alpha_y y] g_n(z), \quad (5.1c)$$

or

$$\phi^{ESS} = \sum_{l,m,n} [a_{lmn}(t) \cos l\alpha_x x \cos m\alpha_y y + \tilde{a}_{lmn}(t) \cos l\alpha_x x \sin m\alpha_y y + a_{lmn}(t) \sin l\alpha_x x \cos m\alpha_y y + a_{lmn}(t) \sin l\alpha_x x \sin l\alpha_y y] g_n(z), \quad (5.1d)$$

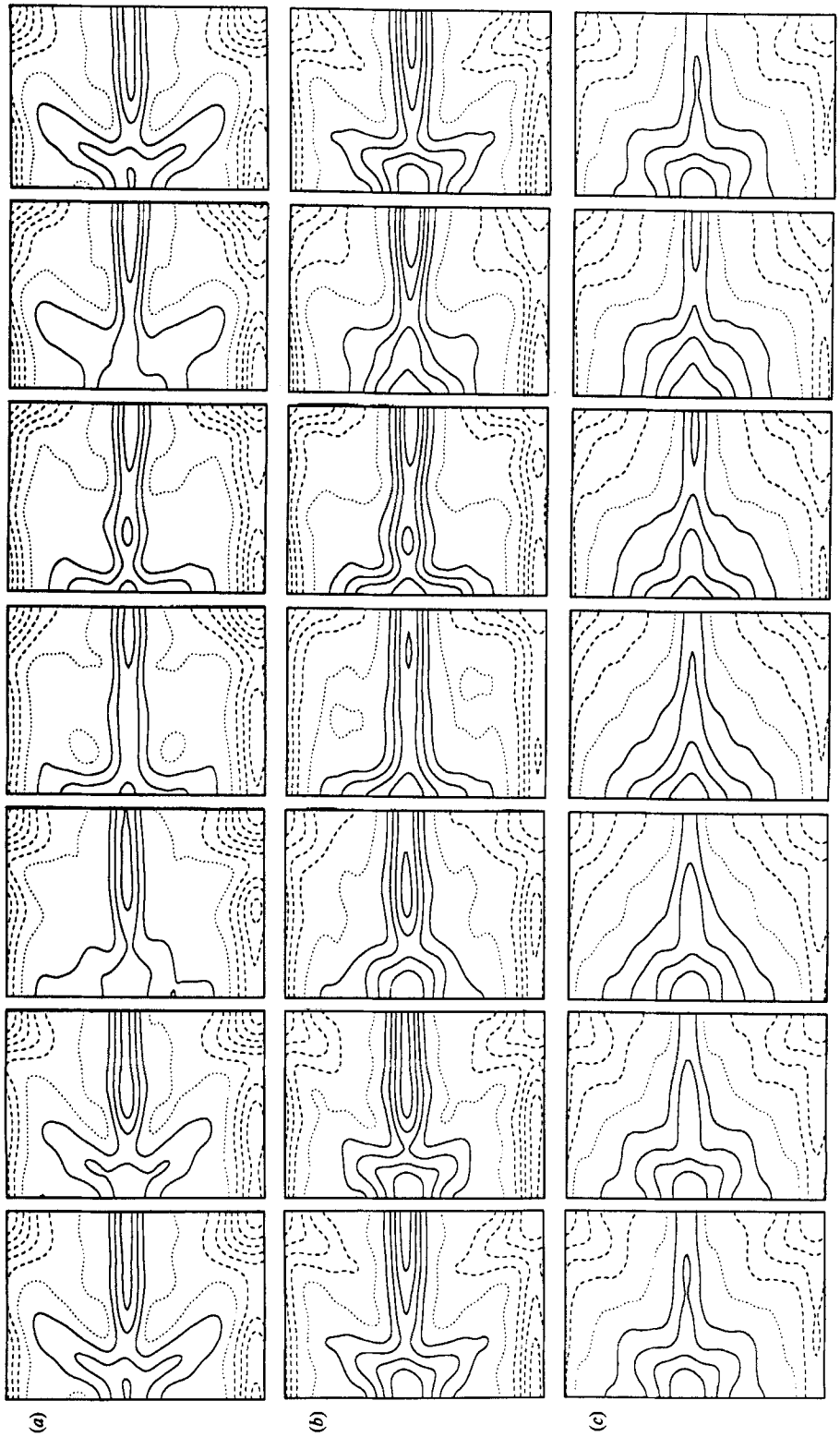

FIGURE 10. Evolution in time of the oscillating knot solution arising from the ECS-instability with unrestricted mean flow in the case $P = 2.5$, $\alpha_x = 1.4, \alpha_y = 2.0$, $R = 3.5 \times 10^4$, $N_T = 10$. Rows (*a*) and (*b*) show lines of constant vertical velocity at $z = -0.3$ and $z = 0$, respectively, and (*c*) shows lines of constant $\int \theta \, dz$. The six equidistant time steps with $\Delta t = 0.015$ cover about one period such that the last picture closely resembles the first one.

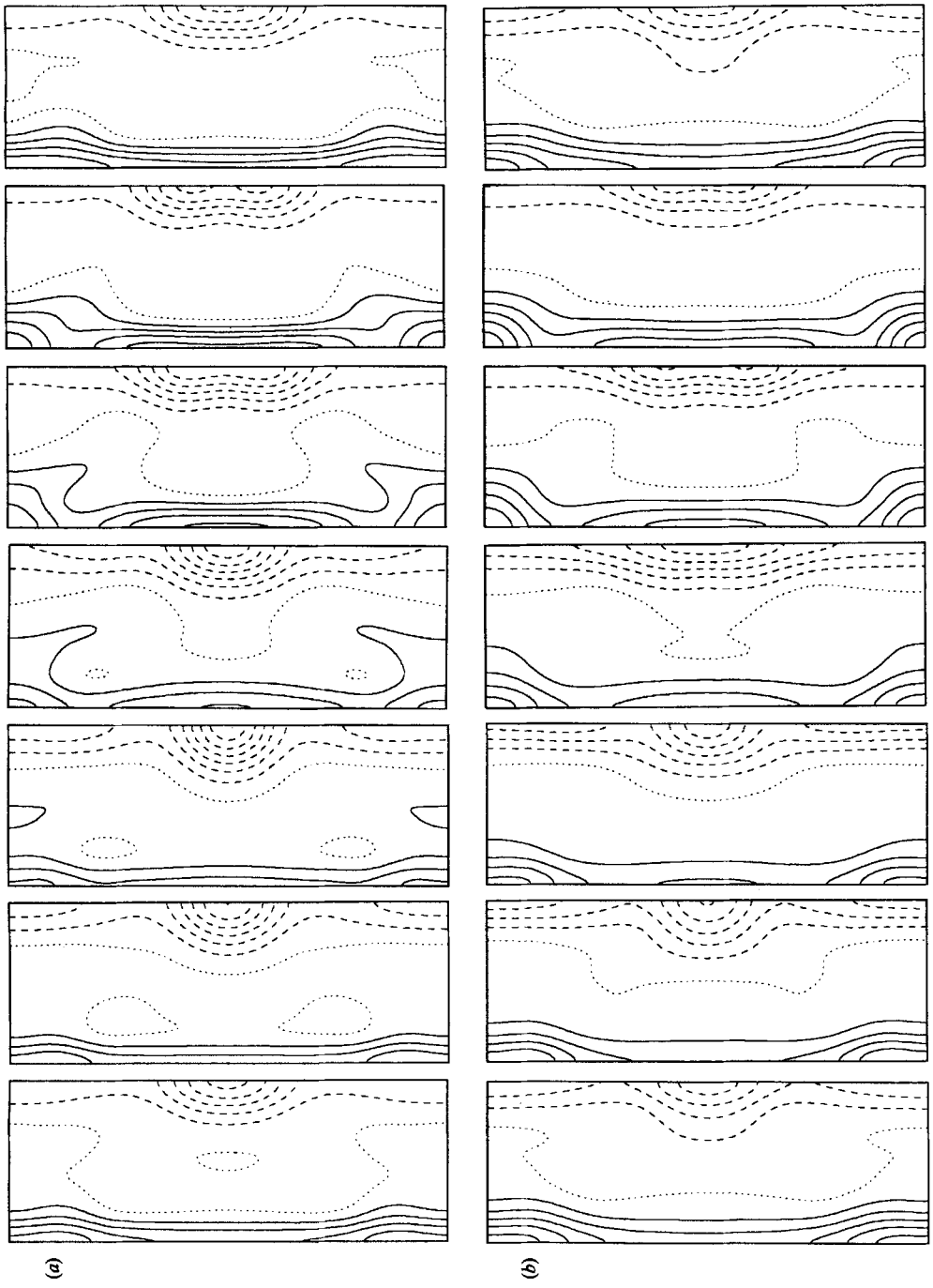

FIGURE 11. Same as figure 10, but arising from the OCC-instability in the case $P = 7.0$, $\alpha_x = 1.8, \alpha_y = 2.5$, $R = 4.5 \times 10^4$, $N_T = 10$ with $\Delta t = 0.008$. The vertically averaged temperature is not shown.

and using analogous replacements for expressions (2.4*b*, *c*), (4.1*a*) we obtain instead of the algebraic equations a system of ordinary differential equations in time. The procedure is the same in the case of the odd instabilities OCC, OSC, OCS, OSS, except that the restriction $l+m+n =$ even must be dropped. Using the semi-implicit Crank–Nicholson scheme for the numerical integration we find that the solutions become periodic in time after initial transients. But the oscillatory part of the solutions always remains a small part of the total solution and – in a time-averaged sense – the oscillatory knot solutions do not differ much from the steady knot solutions.

Because of the computational expenses in following the typically long transients in the evolution of the oscillatory instabilities, we shall restrict our attention to two examples. In figure 10 the case of the ECS-instability for $P = 2.5$ is considered, which occurs at a relatively low Rayleigh number. The comparison of the velocity field at $z = -0.3$ and at $z = 0$ indicates the periodic formation of ridges in the hot thermal boundary layer which are then advected to the central plume. The fairly well preserved symmetry in the y-direction with respect to the position of the rising sheet of fluid is surprising. While the position of the sheet has been shifted slightly from its original position in the centre of the picture there is otherwise little evidence of the 'shifting' property of the ECS-disturbances. It appears that only a small asymmetry is needed to trigger the oscillations which occur as if the horizontal symmetry of the knot solution is preserved. The time-averaged Nusselt number appears to be slightly increased by a fraction of the order of 0.2 %, while the poloidal kinetic energy is decreased by a comparable amount in relation to the corresponding steady solution. A more significant increase of about 20 % is exhibited by the time-averaged toroidal energy E_{tor}, which indicates that the advection of the periodic eruptions from the thermal boundary layer is connected with an increase in the vertical vorticity of motion.

The second example of oscillations is shown in figure 11 for $P = 7$. Since the OCC-instability has induced the transition in this case, the horizontal symmetry remains unchanged. While the eruption of ridges from the boundary layer is noticeable in this case, it is much less pronounced than in the low-Prandtl-number case. Instead the 'breathing' aspect has become stronger. The maximum of the vertical velocity shifts back and forth between the central plume and the central position in the sheet, as is evident in the plane $z = -0.3$. At the midplane of the layer the highest value of the vertical velocity always occurs in the plume, but the velocity in the sheet still varies strongly throughout the period of oscillation.

Obviously the two examples presented here can provide only a rough idea of the rich variety of features to be expected in time-dependent knot convection. Of particular interest for further investigation will be the large-wavenumber cases for which oscillatory instabilities precede the transition to the steady knot solution. The combination of the steady knot solution with the oscillatory properties is likely to produce some striking effects in those cases.

6. Concluding remarks

The oscillatory knot convection discussed in the preceding section is of special importance for the interpretation of experimental observations because it represents a model for spoke-pattern convection. This latter form of convection occurs over a wide range of the Rayleigh number for moderate to larger Prandtl numbers (Busse & Whitehead 1974; Busse 1981). In experiments started with random initial

convections there is no preferred direction for the spoke-pattern cells, unlike the oscillatory knot solution which retains in the form of two unequal directions the memory of the roll solution from which it has originated. Except for this minor point, however, the theoretical solution reflects all qualitative aspects of the observed spoke-pattern cells. The small-scale spokes correspond to thermal ridges which erupt nearly periodically from the thermal boundary layers and move to the central plumes which remain essentially stationary just as they do in figures 10 and 11. When experiments are done with controlled initial conditions, spoke-pattern cells retaining part of the original roll structure are obtained (Busse & Whitehead 1974). Since the experiments are mostly done at higher Prandtl numbers than those considered in this paper, the transition to bimodal cells precedes the transition to spoke-pattern cells. But the latter resemble very closely the oscillatory knot solution as shown in figure 10. The property that the observed spokes are not truly periodic must be attributed to the phenomenon of many competing instabilities which introduces an element of randomness into the observed convection flow.

The fact that the transition to oscillatory knot convection requires a small amount of asymmetry seems to be typical of other transitions as well. McLaughlin & Orszag (1982) noted in their analysis that symmetry-breaking perturbations were needed for the transition to chaotic thermal convection in air. In the present case it is quite clear that the nature of the asymmetry is of secondary importance in that the Rayleigh numbers R_{III} do not differ much for instabilities of different symmetries. It will be of interest to study the further evolution of the oscillatory knot solution in order to determine whether additional breaks of spatial symmetry are needed for a transition to chaotic time dependence.

The research described in this paper has been supported by the Atmospheric Sciences Section of the US National Science Foundation.

REFERENCES

Bolton, E. W., Busse, F. H. & Clever, R. M. 1986 Oscillatory instabilities of convection rolls at intermediate Prandtl numbers. *J. Fluid Mech.* **164**, 469–485.

Busse, F. H. 1967 On the stability of two-dimensional convection in a layer heated from below. *J. Math. Phys.* **46**, 140–150.

Busse, F. H. 1978 Nonlinear properties of convection. *Rep. Prog. Phys.* **41**, 1929–1967.

Busse, F. H. 1981 Transition to turbulence in Rayleigh–Bénard convection. In *Hydrodynamic Instabilities and the Transition to Turbulence* (ed. H. L. Swinney & J. P. Gollub). Topics in Applied Physics, vol. 45, pp. 97–137. Springer.

Busse, F. H. & Clever, R. M. 1979 Instabilities of convection rolls in a fluid of moderate Prandtl number. *J. Fluid Mech.* **91**, 319–335.

Busse, F. H. & Frick, H. 1985 Square pattern convection in fluids with strongly temperature dependent viscosity. *J. Fluid Mech.* **150**, 451–465.

Busse, F. H. & Whitehead, J. A. 1974 Oscillatory and collective instabilities in large Prandtl number convection. *J. Fluid Mech.* **66**, 67–79.

Chandrasekhar, S. 1961 *Hydrodynamic and Hydromagnetic Stability*. Clarendon.

Clever, R. M. & Busse, F. H. 1974 Transition to time-dependent convection. *J. Fluid Mech.* **65**, 625–645.

Clever, R. M. & Busse, F. H. 1987 Nonlinear oscillatory convection. *J. Fluid Mech.* **176**, 403–417.

Curry, J. H., Herring, J. R., Loncaric, J. & Orszag, S. A. 1984 Order and disorder in two- and three-dimensional Bénard convection. *J. Fluid Mech.* **147**, 1–38.

FRICK, H., BUSSE, F. H. & CLEVER, R. M. 1983 Steady three-dimensional convection at high Prandtl number. *J. Fluid Mech.* **127**, 141–153.

GRÖTZBACH, G. 1982 Direct numerical simulation of laminar and turbulent Bénard convection. *J. Fluid Mech.* **119**, 27–53.

LIPPS, F. B. 1976 Numerical simulation of three-dimensional Bénard convection in air. *J. Fluid Mech.* **75**, 113–148.

MCLAUGHLIN, J. B. & ORSZAG, S. A. 1982 Transition from periodic to chaotic thermal convection. *J. Fluid Mech.* **122**, 123–142.